Nanoscale

PAPER

View Article Online
View Journal | View Issue

Cite this: *Nanoscale*, 2026, **18**, 1957

Electron transport through negatively curved nanographenes

Lucía Palomino-Ruiz, *[a,b] Juan P. Mora-Fuentes,†[a] Silvia Castro-Fernandez,[a] Irene R. Márquez, [a,c] Juan M. Cuerva, [a] José Catalán-Toledo,[d] Marta Mas-Torrent, [d] Núria Crivillers, [d] Edmund Leary, [b] Alba Millán, [a] Linda A. Zotti, *[e,f,g] M. Teresa González *[b] and Araceli G. Campaña *[a]

Pristine graphene exhibits unique physical and chemical properties. However, during its fabrication different imperfections are inevitably formed, which can induce changes to the properties of the material. Bottom-up methologies make it possible to synthesise graphene nanostructures incorporating selected defects in different positions. These graphene-like molecules of reduced size are being increasingly used, first as simple models to investigate the impact of different kind of structural defects, and secondly for achieving structures with selected properties for specific purposes. Some of these defects are able to induce curvature in the structure, but their impact on electron transport has scarcely been investigated. We report the first electron-transport study through saddle-shaped nanographenes, including experimental and theoretical perspectives. For the studied systems, we demonstrate that the inclusion of this kind of curvature by means of a tropone ring at the edge of the structure has no significant effect in terms of both single-molecule and self-assembled monolayer conductance, while enhancing solubility and processability considerably when compared to the defect-free analogues. These results aim at finding useful correlations between out-of-plane distortion on nanographenes and the electron transport through them, in view of the increasing interest in processable carbon nanostructures as potential candidates for the next generation of electronic technologies.

Received 24th September 2025,
Accepted 18th December 2025

DOI: 10.1039/d5nr04033g

rsc.li/nanoscale

Introduction

Graphene, with its unique properties and extraordinary potential for various applications in different fields, stands as a remarkable material in contemporary materials science.[1,2] However, achieving perfect and defect-free graphene structures remains a significant challenge. Defects such as non-hexagonal rings are prevalent and can induce curvature in the graphene lattice.[3] While this curvature may enhance certain applications by modifying the electronic properties,[4,5] it poses a concern for electronic applications where structural integrity is paramount.

Nanographenes (NGs) and other extended polycyclic conjugated hydrocarbons (PCHs) are highly attractive compounds for electronic and optoelectronic applications since their properties can be tuned depending on their size, shape, topology and other structural characteristics.[6–8] Some of them have been successfully incorporated into high-performance optoelectronic devices, pointing to promising applications such as organic field-effect transistors[9,10] and phototransistors for data storage devices.[11] NGs also serve as excellent models for investigating the properties of graphene at a reduced scale, with the advantage of offering a well-defined energy gap. Remarkably, their electronic properties at the single-molecule level have been scarcely explored to date. Previous experimental studies are mainly limited to relatively small PCHs (Fig. 1, top) such as pyrene,[12] anthanthrene,[13] perylene dimides (PDIs)[14] and other N-doped analogues,[15] together with some NGs such as hexa-*peri*-hexabenzocoronene (**HBC**) derivatives[16] or oligomers,[17]

[a]*Departamento de Química Orgánica, Facultad de Ciencias, Unidad de Excelencia de Química Aplicada a Biomedicina y Medioambiente (UEQ), Universidad de Granada, 18071 Granada, Spain. E-mail: lucia.palomino@imdea.org, araceligc@ugr.es*
[b]*Fundación IMDEA Nanociencia, 28049 Madrid, Spain. E-mail: teresa.gonzalez@imdea.org*
[c]*Centro de Instrumentación Científica, Universidad de Granada, 18071 Granada, Spain*
[d]*Institut de Ciència de Materials de Barcelona (ICMAB, CSIC), Campus de la UAB s/n, Bellaterra 08193, Spain*
[e]*Departamento de Física Teórica de la Materia Condensada, Universidad Autónoma de Madrid, 28049 Madrid, Spain. E-mail: linda.zotti@uam.es*
[f]*Condensed Matter Physics Center (IFIMAC), Universidad Autónoma de Madrid, 28049 Madrid, Spain*
[g]*Instituto Nicolás Cabrera (INC), Universidad Autónoma de Madrid, 28049 Madrid, Spain*
†Present address: Departamento de Química Orgánica, Centro Singular de Investigación de Química Biológica y Materiales Moleculares, Universidad de Santiago de Compostela, 18071 Santiago de Compostela, Spain.

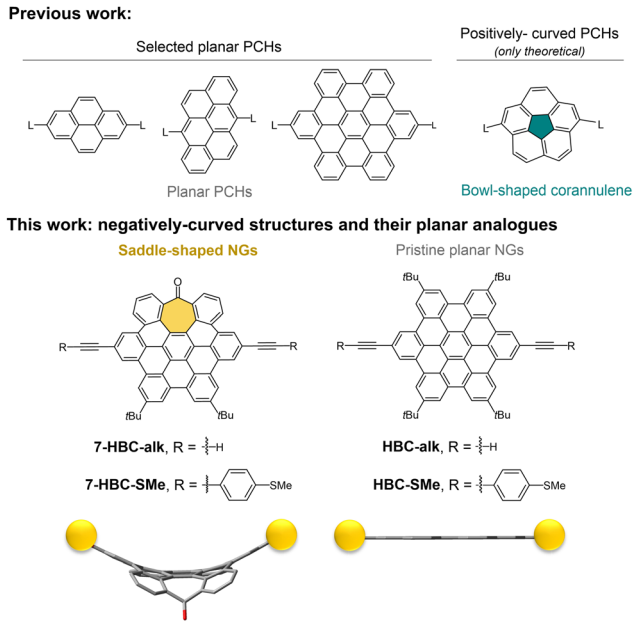

Fig. 1 Top: structures of selected well-defined planar[12,13,16] (left) or bowl-shaped[22] (right) PCHs in which electron transport have been studied (L: represents linkers for electrode anchoring). Bottom: structures of saddle-shaped NGs (left) and planar NGs (right) studied in this work and its representation between gold electrodes (in yellow).

and molecular bilayer-graphene.[18] In particular, curved PCHs, presenting a conjugated sp^2 surface out of the plane, remain almost unexplored in the field, even when it has been probed to present different optical and redox properties when compared to planar systems of similar size.[19] In this sense, the curvature can be induced by the presence of non-hexagonal rings in the structure. Depending on the number of C atoms (n) in these non-hexagonal rings, different types of curvature can be observed. Rings with n = 3–5 generate bowl-shaped (positively-curved) structures, while rings with n = 7–16 lead to saddle-shaped (negatively curved) structures.[20] In contrast, some particular combination of 5- and 7-membered rings are able to cancel the curvature, maintaining planar structures.[21] The electron-transport through positively curved corannulene junctions has only been theoretically studied, finding a higher conductance for alkyne-terminated molecules than for other saturated linkers.[22] Promising spin filter behavior was also predicted for organometallic single-molecule junctions using corannulenes as ligands.[23] Concerning electron-transport through saddle-shaped PCHs, it remains completely unexplored from both experimental and theoretical points of view. The lack of information about the electronic properties of curved NGs makes it difficult to draw consistent assumptions, not only about the impact of curvature on the electron transport properties with respect to defect-free planar structures, but also to predict if these two types of curvature affect differently. This current gap is also surprising, considering curved NGs offer appealing options for organic electronic materials, given their enhanced solubility and processability. In particular, saddle-shaped structures display certain conformational flexibility, in contrast with the rigidity of the bowl-shaped structures, and have potential for novel self-assemblies, different from those occurring in planar counterparts.

In this context, we aim to examine the interplay between defective curved structures and electron transport properties in NGs, thereby providing a deeper understanding of their potential applications in future technologies. Here we report on the electron-transport properties of saddle-shaped NGs (Fig. 1, bottom), in comparison with the corresponding planar pristine analogues. Moreover, we also evaluate the effect of two different anchoring groups. After the stepwise synthesis and full characterization of the target molecules, we experimentally determine that the conductance values of the selected NGs are unaffected by the curvature. We first studied their single-molecule conductance by means of scanning tunneling microscopy break-junction (STM-BJ) technique, which has been extensively used for characterizing electron-transport properties at the single molecule level.[24] These transport measurements are compared with the ones obtained in large molecular junctions using the technique based on the liquid metal eutectic gallium indium alloy (EGaIn) as soft top contact electrode on NGs monolayers.[25] Calculations based on density functional theory (DFT) were performed for evaluating the theoretical conductance values of the molecules, resulting in a better comprehension of the transport phenomena through these systems.

Results and discussion

Design and synthesis of target NGs

The molecular structures of the NGs under study are shown in Fig. 1 (bottom). They are all based on **HBC**, the smaller PCH considered a NG.[26] The negative curvature in the saddle-shaped structures (**7-HBC**-) is promoted by the incorporation of one cycloheptatrienone (tropone) unit at the edge of the **HBC** scaffold. The saddle-shaped distortion induced by this heptagonal ring, has been already demonstrated by X-ray diffraction of similar **7-HBC** structures previously reported in literature.[27] The contrast between the structures of curved **7-HBC** and **HBC** cores is highlighted in Fig. 1 (bottom left and right, respectively). In the planar analogues (**HBC**-), containing only 6-membered rings, four lateral *tert*-butyl (*t*-Bu) groups were introduced in the structure for enhancing the solubility and allowing their characterization. Since the curvature and the ketone group already increase the solubility of the **7-HBC** molecules, only two solubilizing *t*-Bu groups were introduced in this case.

In our study, we have selected two different anchoring groups, which have been included in equivalent positions in both curved and planar analogues. One of the main purposes of the anchoring groups is to create an efficient electronic coupling with the electrodes. Although some previous studies on graphene-related molecules have been conducted without adding anchoring groups,[28–30] they are key for ensuring repro-

ducible and well-defined molecule-electrode contacts. The nature of the linker also plays a fundamental role in the transport, being responsible for changes in conductance of even orders of magnitude for a given molecular backbone. In particular, we have used (i) thiomethyl groups (–SMe),[31–34] linked to the HBC cores through a ethynylbenzene as spacer, and (ii) alkynes (–alk),[35–39] directly bonded to the core. These groups are strategically located on opposite edges of the HBC core to force the electronic current to cross the π-system from one side to the other. The linkers were introduced by Sonogashira coupling from the dibromo (diBr) functionalized **HBC**/**7-HBC** cores, using the corresponding alkyne derivative in each case. Planar diBr-**HBC** was synthesized using a well-established protocol,[40] based on Diels–Alder reaction of diphenylacetylenes with tetraphenylcyclopentadienones, and followed by oxidative cyclodehydrogenation. In the case of the curved diBr-**7-HBC**, its synthesis was also previously reported[41] by a sequence of alkyne cyclotrimerization reactions of adequate precursors, followed by oxidative cyclodehydrogenation.[27] The experimental details and structural characterization of the compounds can be found in the SI, section S1.

Electron-transport studies

We performed room-temperature STM-BJ experiments to characterize the electron transport of these compounds at the single-molecule scale. The variation of the conductance, G, is recorded as the gold tip of the STM is separated, in the z direction, from a gold substrate where the molecule has been previously deposited. This is repeated in successive retract-approach cycles, generating thousands of conductance-distance (G–z) traces. They are studied statistically, obtaining 2D G *vs.* z histograms and 1D G histograms. If no molecular junction is created during the electrode separation, only the typical tunnel current decay is observed. If a molecular junction forms, however, plateaus appear in the G–z traces, giving rise to peaks in the 1D G histograms and areas of high density in the 2D G–z maps (see SI for further details about the technique, sample preparation and data analysis). More than three independent rounds of measurements were performed on freshly prepared samples for each molecule to ensure reproducibility and reliability. For the **7-HBC-SMe**/**HBC-SMe** pair, the percentage of recorded traces that display plateaus was moderate (29–60% for **7-HBC-SMe** and 18–43% for **HBC-SMe**) and, in each measurement round, we collected about 2000 to 7000 traces in total. On the other hand, for the **7-HBC-SMe**/**HBC-alk** pair, the percentage of traces with plateaus was lower (4–12% for **7-HBC-alk** and 4–6% for **HBC-alk**), and we typically collected a total of 11 000–13 000 traces per measurement round. The results obtained for the two pairs of curved and planar molecules with the same anchoring group (**7-HBC-SMe**/**HBC-SMe** pair and **7-HBC-alk**/**HBC-alk** pair) are analyzed independently in the following sections.

7-HBC-SMe/HBC-SMe pair. The 2D histograms (Fig. 2a) for **7-HBC-SMe** and **HBC-SMe** (3613 and 5530 G–z traces, respectively), reveal a very similar profile for both molecules, with a well-defined plateau cloud typical of –SMe terminated

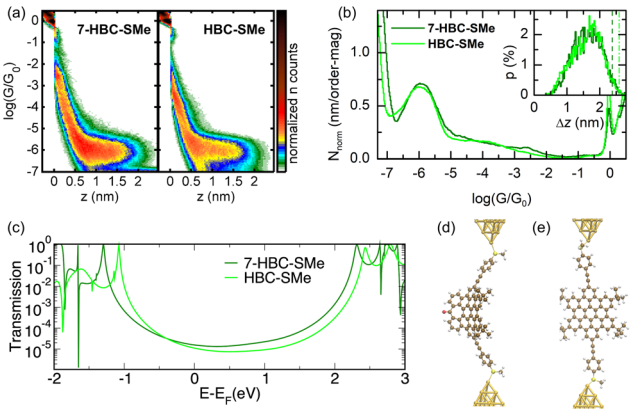

Fig. 2 2D (a) and 1D (b) histograms for **7-HBC-SMe** and **HBC-SMe**. They were built with all the traces displaying plateaus from the different measurement rounds performed for these molecules. Inset in (b) corresponds to the plateau-length distributions. Transmission *versus* Energy (E) curves calculated for **7-HBC-SMe** and **HBC-SMe** (c), in the electrode-molecule-electrode configuration depicted in (d) and (e), respectively.

compounds.[31–34] The signals observed in the 1D histograms (Fig. 2b) show similarities in terms of shape and conductance range, with a mean conductance value of $\log(G/G_0) = -6$ and a full width at half maximum (FWHM) of 1.1 and 1.3, respectively. The close resemblance in behavior was corroborated by applying an additional unsupervised clustering-based analysis of the G–z traces, similar to others previously reported in literature.[42] The result of this analysis is detailed in the SI (Fig. S1 and S2). The plateau-length distribution (Fig. 2b inset) ends near the theoretically expected maximum plateau length, which is 2.54 nm and 2.40 nm for **HBC-SMe** and **7-HBC-SMe**, respectively (marked by vertical dashed lines in the figure inset). The expected maximum plateau length corresponds to the length of the molecule from S to S, plus the S–Au bond distance, minus the typical gold retraction after the gold contact is broken (0.4 nm).[43] I–V traces, ramped along the molecular plateaus in the G–z traces, were also studied for the **7-HBC-SMe**/**HBC-SMe** pair, revealing no appreciable difference in their behavior in the −1.5 V to 1.5 V bias voltage interval (Fig. 3). We conclude therefore that introducing saddle-shaped

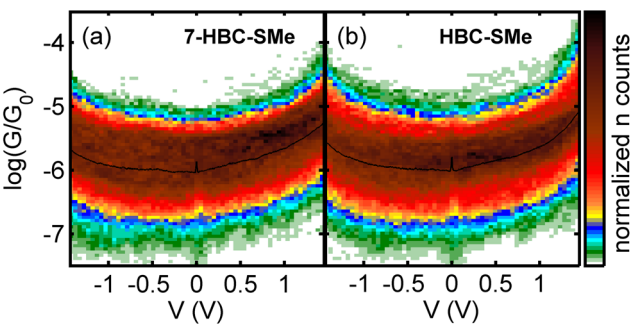

Fig. 3 2D histograms of $\log(G/G_0)$ *vs.* V, built from the −1.5 to +1.5 V ramps along the molecular plateaus for **7-HBC-SMe** (a) and **HBC-SMe** (b).

curvature by inclusion of a tropone unit has no significant effect on the conductance of this NG.

For further insight, we performed computational simulations based on DFT (see details in the SI, section S3). The gas-phase optimized geometry of **7-HBC-SMe** shows an angle of approximately 18° between the planes of two consecutive rings along the backbone axis and 10° in the perpendicular direction. Overall, this gives rise to a total depth of the conjugated core and the whole compound of 1.8 Å and 6.6 Å, respectively, along the longitudinal direction. The gas-phase calculations revealed a very similar spatial distribution of the HOMO in **HBC-SMe** and **7-HBC-SMe**, apart from additional weight on the oxygen in the latter (see Fig. S10). There is also a very close energy alignment of the frontier orbitals of the two compounds (the HOMO (LUMO) of **7-HBC-SMe** being only 0.11 eV (0.18 eV) lower than for **HBC-SMe**). This might be surprising at first, since one would expect the bending in the curved structure to raise both HOMO and LUMO.[44] This would be a consequence of the symmetry breaking of the π system between the regions above and below the molecular plane, which in turn breaks the conjugation uniformity, slightly destabilizing the system.

Previous calculations in the literature focused on bending compounds rather than comparing compounds where curvature has been created by chemical manipulation. In particular, in PCHs, bending is known to shift the frontier orbitals in different ways. For example, in the case of bent acenes, both HOMO and LUMO shift to higher energies,[44] while for PDIs,[45,46] the HOMO energy increases while the LUMO energy decreases upon bending. For pyrenacenes, however, the opposite with respect to PDIs is predicted,[47] due to a bonding interaction arising between the orbital lobes as they approach each other upon bending. Following the same reasoning about the HOMO lobes for **7-HBC-SMe** (Fig. S10), an antibonding interaction would be expected, since the curvature of the structure enhances the interaction between certain lobes of opposite phases along the transport direction. The system would thus destabilize and, in turn, raise the HOMO energy with respect to that of **HBC-SMe**. That said, several factors will counteract this effect, considering that the negative curvature in our system requires structural modification of the pristine planar analogue, rather than a simple bending. Firstly, the presence of the electron-withdrawing carbonyl group is expected to pull the levels down.[48,49] Secondly, this group breaks direct conjugation between two adjacent phenyl rings, which would tend to widen the HOMO–LUMO gap. This is evidenced by the energetics resulting from replacing the CO group with a CH_2 group, which can be regarded as the minimal chemical modification (Table S3 and Fig. S17 in section S3.3.3. of the SI).

In Fig. 2c, we report the transmission curves computed for metal–molecule–metal junctions based on the two compounds. Since the –SMe group prefers binding to undercoordinated gold atoms,[50] the molecules were placed in ideal top-binding positions (Fig. 2d and e). The computed curves were obtained *via* a combination of DFT and Green's function techniques[51,52] (see section S3 of the SI for further details on the methodology and additional computational analyses of the systems). We observe that, in both cases, the transport takes place through the tail of the HOMO, the energetic position of which reflects the same trend found in the gas phase, albeit with a slightly larger shift between the two compounds (by 0.1 eV, probably due to structural re-adjustment taking place in the geometry optimization). The transmission values are very similar for energies in the range ±0.5 eV around the Fermi level. This is partially due to the proximity of the two HOMO resonances with respect to each other, and partially to the equal energetic distance between HOMO and LUMO resonances. This results in the two transmission curves crossing near the Fermi level. Thus, the molecular conductance (given, to a good approximation, by the transmission at this energy) is found to be very similar (1.6×10^{-5} G_0 and 1.1×10^{-5} G_0 for **7-HBC-SMe** and **HBC-SMe**, respectively). Such behavior is consistent with the experimental results discussed above, which showed similar conductance for the two compounds. The similarity in the **7-HBC-SMe**/**HBC-SMe** pair is also consistent with predictions obtained by tight-binding (TB) approaches (SI, section S3.2).

In order to investigate the effect of the lateral π-extension and conjugation in the electron transport, we synthetized the heptagon-containing hexaphenylbenzene (HPB) analogue **7-HPB-SMe** (see SI, Scheme S4). This compound has a similar size but is less conjugated than **7-HBC-SMe**, as the additional C–C bonds responsible for creating the **HBC** core are missing. The results of the STM-BJ experiments for this molecule are available in Fig. S4. The 2D histogram (Fig. S4a) reveals a single well-defined conductance signal that starts below −6 log (G/G_0) and extends beyond the limits of the experimental detection window, with a mean conductance of about 1.5 orders of magnitude lower than that of **7-HBC-SMe**. No signals compatible with through-space conjugation were observed in this case, as has been previously reported for other HPB-based molecules.[53] The plateau length distributions concur at the same values for both molecules (Fig. S4b), in agreement with their almost identical expected linker-to-linker distances (see Table S1). The experimental conductance decrease observed for **7-HPB-SMe** with respect to **7-HBC-SMe**, agrees with the computed transmission curves (Fig. S15d). A closer inspection of the optimized junction geometries (Fig. 2d and Fig. S15a) allows us to relate this conductance change with the different dihedral angles in the central moiety, going from 63° in the **7-HPB-SMe** to near zero in **7-HBC-SMe** (see section S3.3.1. of the SI for further discussion). These results show that the lateral extension of conjugation is a good strategy for increasing the conductance while maintaining the length, as long as it is associated with limiting the torsion angles along the conduction pathway.

7-HBC-alk/HBC-alk pair. This pair allowed us to investigate if the similarities in electrical behavior for curved and planar HBCs are also present when there is a considerably stronger coupling with the electrodes, taking into account that previous studies have estimated the rupture force of the C–Au bond to be approximately 3 times higher than that of S–Au.[36]

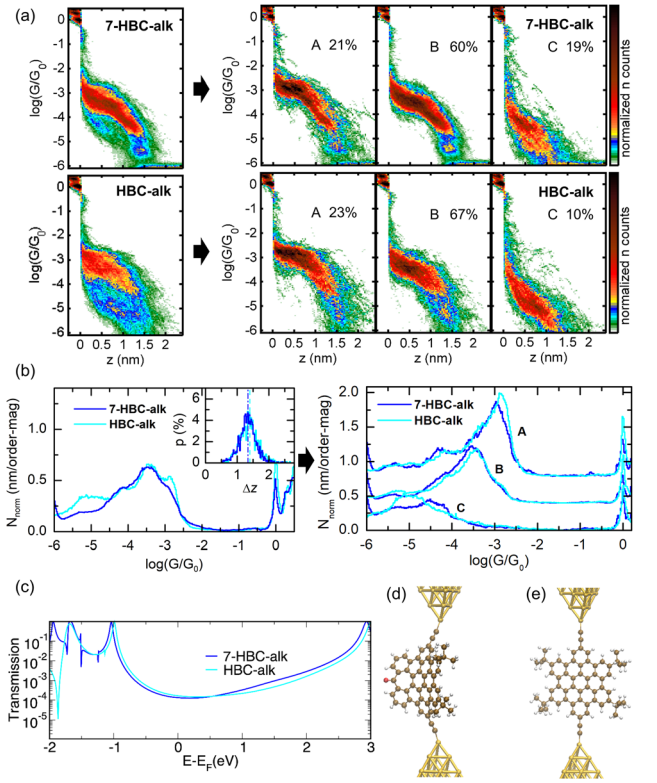

Fig. 4 2D (a) and 1D (b) histograms for **7-HBC-alk** and **HBC-alk** before (left) and after (right) a cluster-based analysis (indicated by a black arrow). The histograms before the clustering analysis (left) correspond to all the traces displaying plateaus from only one measurement round for each molecule. Inset in b-left corresponds to the plateau-length distributions considering all the traces, while the distribution obtained for each group are available in the Fig. S7. (c) Transmission curves predicted by DFT (see SI, section S3 for details), corresponding to the junction geometries in (d) and (e) for **7-HBC-alk** and **HBC-alk**, respectively. For homogeneity, top-binding geometries, similar to those analysed for the SMe-terminated compounds, were considered.

2D and 1D histograms built from the G–z traces showing plateaus for **7-HBC-alk** and **HBC-alk** are available in Fig. 4a and b (950 G–z traces, 7% success rate, and 844 G–z traces, 4% success rate, respectively), and display a very different molecular signal than that obtained for the –SMe terminated pair. The histograms reveal a multi-peak molecular signal that expands for more than 3 orders of magnitude. Multi-peak signals are normally an indication of various processes occurring in the junction while stretching the electrodes. This kind of profile, typically observed for compounds with terminal alkyne groups,[35–39] can be difficult to interpret without further data analysis. For a deeper understanding of this behavior, a clustering-based analysis was applied to the data, indicated in Fig. 4a and b with a black arrow. In this analysis, we could distinguish three groups (A, B and C) within the G–z traces with plateaus for **7-HBC-alk** and **HBC-alk**.

Clearly, the observations in terms of histogram profiles, conductance values and plateau lengths for the three groups for **7-HBC-alk** and **HBC-alk** are very similar. This result confirms that inducing curvature in the system by the applied structural changes is not translated into a loss of electron transport potential at the single-molecule level, regardless of the selected anchoring group and, therefore, independently of the coupling strength with the electrodes.

For both compounds, groups A and B display flat plateaus followed by a bulged conductance fall. This drastic change in the trace profile is an indication of a transition between different processes during the breakdown of the junction. The length distributions until the end of the flat region and until the end of the bulged tail suggest that the former corresponds to the formation of a stable molecular junction, while the latter is due to rearrangements of the gold prior to the junction breakage, in agreement with previous theoretical[54] and experimental[35] work with ethynyl-terminated molecules. The conductance values for this flatter region are slightly higher in group A ($\log(G/G_0) = -3$) than in group B ($\log(G/G_0) = -3.5$), suggesting that they are generated by two slightly different stable junctions. The most plausible hypothesis relates them with the different ways of bonding that have been reported for Au and acetylene groups, involving not only σ/σ interactions, but also σ/π and π/π.[55] The third group (C), is formed by sloping traces, going towards lower conductance values.

The transmission curves obtained by DFT (Fig. 4c), as well as TB calculation (Fig. S13), support once more the experimental similarities between the flat and curved compounds. In addition, they predict higher conductance for the ethynyl-terminated compounds with respect to the longer ethynylbenzene-SMe counterparts, in agreement with the general experimental trend. The difference between the theoretical values for the two types of binding is approximately one order of magnitude, in agreement with the difference in length, although slightly lower than observed experimentally. The large experimental distribution in conductance suggests that more geometrical configurations other than those shown in Fig. 4d and e are at play. For instance, it was reported that terminal alkynes prefer to bind to gold in bridge positions.[36,55] In addition, binding geometries involving the aforementioned σ/π and π/π interaction at the metal–molecule interface may also be formed. Considering the relative theoretical difference between –SMe and alkyne groups implies that the geometries analysed in Fig. 4d and e fit in the lower tail of the experimental distribution. Conversely, the transmission curves computed for the alkyne family in the bridge binding position (Fig. S16) show higher conductance values than in the top configuration and could thus correspond to the higher-conductance experimental plateaus. Remarkably, placing the flat and curved compounds in identical binding geometries results, again, in similar conductance values. That said, a precise assignment of experimental conductance groups to specific binding geometries would require an extensive computational study covering a much larger variety of structures at different stretching stages. This goes well beyond the bounds of this work. A more detailed analysis and further discussion about the three conductance groups can be found in the SI.

Electron-transport through self-assembled monolayers (SAMs). In order to test if intermolecular interactions have a

different effect on the transport properties of **HBC** and **7-HBC** compounds, we extended our studies to SAMs of the four different derivatives. These were prepared on smooth template-stripped Au (Au^{TS})[56] surfaces, by immersing the bare Au in a chlorobenzene solution of the respective compounds (see SI, section S4 for further details). First, the resulting modified electrodes were characterized by cyclic voltammetry (CV) using $[Fe(CN)_6]^{3-/4-}$ as redox probe. The results revealed that the Au substrates were passivated by the organic monolayer since the redox peak intensity associated with the $[Fe(CN)_6]^{3-}$/$[Fe(CN)_6]^{4-}$ redox couple diminished after the SAM formation. This was ascribed to a poorer electron transfer efficiency from the redox probe in the solution to the electrode compared with the bare gold (Fig. S18). For both pairs of molecules, the hexagonal planar derivatives (**HBC-SMe** and **HBC-alk**) showed a lower current intensity in their CV, indicating higher coverage than the curved derivatives (**7-HBC-SMe** and **7-HBC-alk**). This effect could be associated to a better molecule packaging in the monolayer based on the lateral π–π interactions being more favoured between **HBC** than between **7-HBC** cores.

Subsequently, charge transport measurements were performed using the liquid metal EGaIn as top electrode, giving EGaIn/GaOx/SAMs/Au^{TS} large area junctions. The EGaIn metal can be shaped as a tip to soft-contact organic layer and it has been previously employed to measure the transport through a wide variety of molecular monolayers,[57,58] including SAMs composed of conjugated molecules.[25] As shown in Fig. S19, similar $\log|J|$ values were measured for each pair of SAMs, indicating that the curvature does not affect the measured current density values, which is in agreement with the results described above for single-molecule junctions. It is therefore shown again that this kind of structural defects does not affect the electron-transport in graphene-like molecules, while being beneficial for processability, adsorption or electrochemical properties.

Conclusions

We have investigated the electron transport properties of negatively curved HBC-like NGs using two complementary approaches: break-junctions for single-molecule studies and EGaIn drop for self-assembled monolayer characterization. Two different binding groups have been used (namely terminal –SMe and alkyne groups), involving weaker and stronger coupling with the electrodes, respectively. In all cases, we have observed no significant change in the electrical properties of these molecules with respect to their corresponding planar counterparts, in agreement with our theoretical DFT and TB calculations. Our results demonstrate that the introduction of negative curvature by inclusion of a tropone ring in an HBC core does not degrade the electron-transport properties neither at single-molecule level nor in bulk as SAMs. Therefore, this strategy could be considered as an advanced alternative to traditional planar PCHs, enhancing their processability without compromising their electronic behavior. Structural defects in graphene-related molecules are generally considered as a problem for electronic applications as they are usually associated with low charge carrier mobility and higher resistivity. However, our results demonstrate that this is not always the case, pointing out at the importance of shedding light on the impact of structural defects on different properties. These findings would allow the smart design of graphene-like structures for specific purposes, going a step further towards their real application in the next generation of carbon-based materials. We note, however, that structural changes, such as the position of the anchoring groups and the way of inducing the curvature, can play a different role in terms of the electron-transport properties depending on the particular system under study. We hope our findings will encourage the community to explore new out-of-the-plane systems in the near future, in order to further unravel all the implications of curvature on the electrical properties of PCHs and exploit its potential.

Author contributions

Conceptualization: A. G. C., J. M. C., A. M., M. T. G.; funding acquisition: A. G. C., J. M. C., M. T. G., M. M.-T., N. C., L. A. Z.; supervision: A. G. C., J. M. C., A. M., M. T. G., M. M.-T., N. C., L. A. Z.; project administration: A. G. C., M. T. G., L. A. Z.; investigation: L. P.-R., J. P. M.-F., S. C.-F., I. R. M., J. C.-T., L. A. Z., E. L.; methodology: L. P.-R., S. C.-F., I. R. M, J. C.-T., L. A. Z., E. L.; validation: L. P.-R., J. P. M.-F., S. C.-F., I. R. M., L. A. Z., E. L.; data curation: M. T. G., L. P.-R., L. A. Z.; formal analysis: M. T. G., L. P.-R., I. R. M., J. C.-T., L. A. Z., E. L.; writing original draft: L. P.-R., A. G. C., A. M., M. T. G., L. A. Z.; review & editing: all authors.

Conflicts of interest

There are no conflicts to declare.

Data availability

The data underlying this study are available at Imdea Nanociencia institutional repository, at https://repositorio.imdeananociencia.org/entities/publication/4f240bd9-dccd-4a15-b96d-616b72cd16f7.

Supplementary Information (SI): synthesis and full characterisation of compounds; experimental details of STM-BJ and EGaIn techniques and further measurements; further details on DFT and TB calculations. See DOI: https://doi.org/10.1039/d5nr04033g.

Acknowledgements

We acknowledge grants PID2021-127521NB-I00, PID2021-125604NB-I00, PID2022-141393OB-I00, PID2021-127964NB-C21 and PID2021-127964NB-C22, funded by MICIU/AEI/10.13039/501100011033 and by "ERDF/EU". We thank the

"Severo Ochoa" Programme for Centers of Excellence in R&D (CEX2020-001039-S and CEX2023-001263-S), the "María de Maeztu" Programme for Units of Excellence in R&D (CEX2023-001316-M) and the Generalitat de Catalunya (2021-SGR-00443). Authors also thank DECOSMOL (EIGConcertJapan, PCI2023-143389). I. R. M. acknowledges grant B-CIC-034-UGR23 funded by Consejería de Universidad, Investigación e Innovación and by ERDF Andalusia Program 2021–2027. J. C.-T. is enrolled in the UAB Chemistry PhD program and thanks the DOC-FAM Fellowship, grant agreement no. 754397 through H2020-MSCA-COFUND-2016. L. A. Z. thanks the Spanish MICIU/AEI/10.13039/501100011033 for the grant CNS2024-154593. E. L. acknowledges the grant CNS2023-145464 funded by MICIU/AEI/10.13039/501100011033 and by EU NextGenerationEU/PRTR. Funding for open access charge: Universidad de Granada.

References

1 K. S. Novoselov, A. K. Geim, S. V. Morozov, D. Jiang, Y. Zhang, S. V. Dubonos, I. V. Grigorieva and A. A. Firsov, *Science*, 2004, **306**, 666–669.
2 P. Izquierdo-García, J. M. Fernández-García and N. Martín, *J. Am. Chem. Soc.*, 2024, **146**, 32222–32234.
3 M. D. Bhatt, H. Kim and G. Kim, *RSC Adv.*, 2022, **12**, 21520–21547.
4 S. Tang, L. Xu, K. Dong, Q. Wang, J. Zeng, X. Huang, H. Li, L. Xia and L. Wang, *Appl. Surf. Sci.*, 2023, **615**, 156357.
5 W. Yan, W. Y. He, Z. D. Chu, M. Liu, L. Meng, R. F. Dou, Y. Zhang, Z. Liu, J. C. Nie and L. He, *Nat. Commun.*, 2013, **4**, 1–7.
6 A. Narita, X. Y. Wang, X. Feng and K. Müllen, *Chem. Soc. Rev.*, 2015, **44**, 6616–6643.
7 Z. Liu, S. Fu, X. Liu, A. Narita, P. Samorì, M. Bonn and H. I. Wang, *Adv. Sci.*, 2022, **9**, 1–18.
8 Y. Gu, Z. Qiu and K. Müllen, *J. Am. Chem. Soc.*, 2022, **144**, 11499–11524.
9 K. Schmoltner, F. Schlütter, M. Kivala, M. Baumgarten, S. Winkler, R. Trattnig, N. Koch, A. Klug, E. J. W. List and K. Müllen, *Polym. Chem.*, 2013, **4**, 5337–5344.
10 K. Matsuo, S. Saito and S. Yamaguchi, *Angew. Chem., Int. Ed.*, 2016, **55**, 11984–11988.
11 S. Bai, L. Yang, K. Haase, J. Wolansky, Z. Zhang, H. Tseng, F. Talnack, J. Kress, J. P. Andrade, J. Benduhn, J. Ma, X. Feng, M. Hambsch and S. C. B. Mannsfeld, *Adv. Sci.*, 2023, **10**, 1–12.
12 S. Sangtarash, C. Huang, H. Sadeghi, G. Sorohhov, J. Hauser, T. Wandlowski, W. Hong, S. Decurtins, S. X. Liu and C. J. Lambert, *J. Am. Chem. Soc.*, 2015, **137**, 11425–11431.
13 Y. Geng, S. Sangtarash, C. Huang, H. Sadeghi, Y. Fu, W. Hong, T. Wandlowski, S. Decurtins, C. J. Lambert and S. X. Liu, *J. Am. Chem. Soc.*, 2015, **137**, 4469–4476.
14 B. Xu, X. Xiao, X. Yang, L. Zang and N. Tao, *J. Am. Chem. Soc.*, 2005, **127**, 2386–2387.
15 H. Zhang, P. Zhou, A. Daaoub, S. Sangtarash, S. Zhao, Z. Yang, Y. Zhou, Y. L. Zou, S. Decurtins, R. Häner, Y. Yang, H. Sadeghi, S. X. Liu and W. Hong, *Chem. Sci.*, 2023, **14**, 6079–6086.
16 I. Diez-Perez, Z. Li, J. Hihath, J. Li, C. Zhang, X. Yang, L. Zang, Y. Dai, X. Feng, K. Muellen and N. Tao, *Nat. Commun.*, 2010, **1**, 31.
17 M. Zhang, B. Wang, H. Jia, C. Zhao, J. Hao, W. Liu, L. Zhou, E. Zhang, Y. Chen, P. Du, J. Wang, C. Jia and X. Guo, *ACS Mater. Lett.*, 2024, **6**, 4388–4394.
18 S. Zhao, Z. Y. Deng, S. Albalawi, Q. Wu, L. Chen, H. Zhang, X. J. Zhao, H. Hou, S. Hou, G. Dong, Y. Yang, J. Shi, C. J. Lambert, Y. Z. Tan and W. Hong, *Chem. Sci.*, 2022, **13**, 5854–5859.
19 K. Kawasumi, Q. Zhang, Y. Segawa, L. T. Scott and K. Itami, *Nat. Chem.*, 2013, **5**, 739–744.
20 M. Rickhaus, M. Mayor and M. Juríček, *Chem. Soc. Rev.*, 2017, **46**, 1643–1660.
21 Y. Fei and J. Liu, *Adv. Sci.*, 2022, **9**, 1–23.
22 L. Zoppi, A. Ferretti and K. K. Baldridge, *J. Chem. Theory Comput.*, 2015, **11**, 4900–4910.
23 Y. Jiang, X. Xu, Y. Hu, G. Zhang, Z. Liang, W. Li, Y. Jiang and X. Sun, *Phys. Chem. Chem. Phys.*, 2018, **20**, 20280–20286.
24 T. Fu, K. Frommer, C. Nuckolls and L. Venkataraman, *J. Phys. Chem. Lett.*, 2021, **12**, 10802–10807.
25 R. C. Chiechi, E. A. Weiss, M. D. Dickey and G. M. Whitesides, *Angew. Chem., Int. Ed.*, 2008, **47**, 142–144.
26 L. Chen, Y. Hernandez, X. Feng and K. Müllen, *Angew. Chem., Int. Ed.*, 2012, **51**, 7640–7654.
27 I. R. Márquez, N. Fuentes, C. M. Cruz, V. Puente-Muñoz, L. Sotorrios, M. L. Marcos, D. Choquesillo-Lazarte, B. Biel, L. Crovetto, E. Gómez-Bengoa, M. T. González, R. Martin, J. M. Cuerva and A. G. Campaña, *Chem. Sci.*, 2017, **8**, 1068–1074.
28 J. Zhang, L. Qian, G. B. Barin, A. H. S. Daaoub, P. Chen, K. Müllen, S. Sangtarash, P. Ruffieux, R. Fasel, H. Sadeghi, J. Zhang, M. Calame and M. L. Perrin, *Nat. Electron.*, 2023, **6**, 572–581.
29 N. Richter, Z. Chen, A. Tries, T. Prechtl, A. Narita, K. Müllen, K. Asadi, M. Bonn and M. Kläui, *Sci. Rep.*, 2020, **10**, 1–8.
30 M. Koch, F. Ample, C. Joachim and L. Grill, *Nat. Nanotechnol.*, 2012, **7**, 713–717.
31 Y. S. Park, A. C. Whalley, M. Kamenetska, M. L. Steigerwald, M. S. Hybertsen, C. Nuckolls and L. Venkataraman, *J. Am. Chem. Soc.*, 2007, **129**, 15768–15769.
32 D. Miguel, L. Álvarez de Cienfuegos, A. Martín-Lasanta, S. P. Morcillo, L. A. Zotti, E. Leary, M. Bürkle, Y. Asai, R. Jurado, D. J. Cárdenas, G. Rubio-Bollinger, N. Agraït, J. M. Cuerva and M. T. González, *J. Am. Chem. Soc.*, 2015, **137**, 13818–13826.
33 Y. Tang, Y. Zhou, D. Zhou, Y. Chen, Z. Xiao, J. Shi, J. Liu and W. Hong, *J. Am. Chem. Soc.*, 2020, **142**, 19101–19109.

34 R. Casares, Á. Martínez-Pinel, S. Rodríguez-González, I. R. Márquez, L. Lezama, M. T. González, E. Leary, V. Blanco, J. G. Fallaque, C. Díaz, F. Martín, J. M. Cuerva and A. Millán, *J. Mater. Chem. C*, 2022, **10**, 11775–11782.
35 W. Hong, H. Li, S. X. Liu, Y. Fu, J. Li, V. Kaliginedi, S. Decurtins and T. Wandlowski, *J. Am. Chem. Soc.*, 2012, **134**, 19425–19431.
36 F. Bejarano, I. J. Olavarria-Contreras, A. Droghetti, I. Rungger, A. Rudnev, D. Gutiérrez, M. Mas-Torrent, J. Veciana, H. S. J. Van Der Zant, C. Rovira, E. Burzurí and N. Crivillers, *J. Am. Chem. Soc.*, 2018, **140**, 1691–1696.
37 R. Davidson, O. A. Al-Owaedi, D. C. Milan, Q. Zeng, J. Tory, F. Hartl, S. J. Higgins, R. J. Nichols, C. J. Lambert and P. J. Low, *Inorg. Chem.*, 2016, **55**, 2691–2700.
38 G. Mitra, V. Delmas, H. Al Sabea, L. Norel, O. Galangau, S. Rigaut, J. Cornil, K. Costuas and E. Scheer, *Nanoscale Adv.*, 2022, **4**, 457–466.
39 J. R. Deng, M. T. González, H. Zhu, H. L. Anderson and E. Leary, *J. Am. Chem. Soc.*, 2024, **146**, 3651–3659.
40 M. M. Martin, D. Lungerich, P. Haines, F. Hampel and N. Jux, *Angew. Chem., Int. Ed.*, 2019, **58**, 8932–8937.
41 S. Castro-Fernández, C. M. Cruz, I. F. A. Mariz, I. R. Márquez, V. G. Jiménez, L. Palomino-Ruiz, J. M. Cuerva, E. Maçôas and A. G. Campaña, *Angew. Chem., Int. Ed.*, 2020, **59**, 7139–7145.
42 D. Cabosart, M. El Abbassi, D. Stefani, R. Frisenda, M. Calame, H. S. J. Van der Zant and M. L. Perrin, *Appl. Phys. Lett.*, 2019, **114**, 143102.
43 C. R. Arroyo, E. Leary, A. Castellanos-Gómez, G. Rubio-Bollinger, M. T. González and N. Agraït, *J. Am. Chem. Soc.*, 2011, **133**, 14313–14319.
44 A. M. Armon, A. Bedi, V. Borin, I. Schapiro and O. Gidron, *Eur. J. Org. Chem.*, 2021, **2021**, 5424–5429.
45 F. S. Conrad-Burton, T. Liu, F. Geyer, R. Costantini, A. P. Schlaus, M. S. Spencer, J. Wang, R. H. Sánchez, B. Zhang, Q. Xu, M. L. Steigerwald, S. Xiao, H. Li, C. P. Nuckolls and X. Zhu, *J. Am. Chem. Soc.*, 2019, **141**, 13143–13147.
46 T. Liu, J. Yang, F. Geyer, F. S. Conrad-Burton, R. Hernández Sánchez, H. Li, X. Zhu, C. P. Nuckolls, M. L. Steigerwald and S. Xiao, *Angew. Chem., Int. Ed.*, 2020, **59**, 14303–14307.
47 C. M. Cruz, J. C. Walsh and M. Juríček, *Org. Mater.*, 2022, **4**, 163–169.
48 A. Alanazy, E. Leary, T. Kobatake, S. Sangtarash, M. T. González, H. W. Jiang, G. R. Bollinger, N. Agräit, H. Sadeghi, I. Grace, S. J. Higgins, H. L. Anderson, R. J. Nichols and C. J. Lambert, *Nanoscale*, 2019, **11**, 13720–13724.
49 L. A. Zotti and E. Leary, *Phys. Chem. Chem. Phys.*, 2020, **22**, 5638–5646.
50 M. Kamenetska, M. Koentopp, A. C. Whalley, Y. S. Park, M. L. Steigerwald, C. Nuckolls, M. S. Hybertsen and L. Venkataraman, *Phys. Rev. Lett.*, 2009, **102**, 126803.
51 F. Pauly, J. K. Viljas, U. Huniar, M. Häfner, S. Wohlthat, M. Bürkle, J. C. Cuevas and G. Schön, *New J. Phys.*, 2008, **10**, 125019.
52 L. A. Zotti, M. Bürkle, F. Pauly, W. Lee, K. Kim, W. Jeong, Y. Asai, P. Reddy and J. C. Cuevas, *New J. Phys.*, 2014, **16**, 015004.
53 S. Zhen, J. C. Mao, L. Chen, S. Ding, W. Luo, X. S. Zhou, A. Qin, Z. Zhao and B. Z. Tang, *Nano Lett.*, 2018, **18**, 4200–4205.
54 R. C. Hoft, M. J. Ford and V. M. Garc, *J. Phys.: Condens. Matter*, 2008, **20**, 025207.
55 P. Maity, S. Takano, S. Yamazoe, T. Wakabayashi and T. Tsukuda, *J. Am. Chem. Soc.*, 2013, **135**, 9450–9457.
56 E. A. Weiss, G. K. Kaufman, J. K. Kriebel, Z. Li, R. Schalek and G. M. Whitesides, *Langmuir*, 2007, **23**, 9686–9694.
57 Y. Liu, L. Ornago, M. Carlotti, Y. Ai, M. El Abbassi, S. Soni, A. Asyuda, M. Zharnikov, H. S. J. van der Zant and R. C. Chiechi, *J. Phys. Chem. C*, 2020, **124**, 22776–22783.
58 Y. Zhang, G. Ye, S. Soni, X. Qiu, T. L. Krijger, H. T. Jonkman, M. Carlotti, E. Sauter, M. Zharnikov and R. C. Chiechi, *Chem. Sci.*, 2018, **9**, 4414–4423.